



A Search for Black Hole Microlensing Signatures in Globular Cluster NGC 6656 (M22)

N. Kains^{1,2}, A. Calamida¹, K. C. Sahu¹, J. Anderson¹, S. Casertano¹, and D. M. Bramich³

¹Space Telescope Science Institute, 3700 San Martin Drive, Baltimore, MD 21218, USA
²Department of Physics & Astronomy, Barnard College, Columbia University, 3009 Broadway, New York, NY 10027, USA
³New York University Abu Dhabi, PO Box 129188, Saadiyat Island, Abu Dhabi, UAE

Received 2018 June 13; revised 2018 September 13; accepted 2018 September 18; published 2018 October 29

Abstract

We report the results of a study aiming to detect signs of astrometric microlensing caused by an intermediate-mass black hole (IMBH) in the center of globular cluster M22 (NGC 6656). We used archival data from the *Hubble Space Telescope* (*HST*) taken between 1995 and 2014 to derive long-baseline astrometric time series for stars near the center of the cluster, using state-of-the-art software to extract high-precision astrometry from images. We then modeled these time-series data and compared microlensing model fits to simple linear proper-motion fits for each selected star. We find no evidence for astrometric microlensing in M22, in particular for bulge stars, which are much more likely to be lensed than cluster stars, due to the geometry of microlensing events. Although it is in principle possible to derive mass limits from such nondetections, we find that no useful mass limits can be derived for M22 with available data, mostly due to a 10 year gap in coverage. This is a result from difficulties with deriving precise enough astrometry from Wide Field Planetary Camera 2 observations for stars that do not fall on the planetary camera chip. However, this study shows that, for other *HST* instruments, we are able to reach precisions at which astrometric microlensing signals caused by IMBH in globular clusters could be detected and that this technique is a promising tool to make a first unambiguous detection of an IMBH.

Key words: astrometry – globular clusters: individual (M22, NGC 6656) – gravitational lensing: micro – proper motions – stars: black holes

1. Introduction

The formation of supermassive black holes (SMBHs) in the early universe is one of the most debated issues in modern astronomy. Indeed, SMBHs are found at large redshifts, meaning that some of them had already formed only a few hundred million years after the Big Bang (Fan 2006). However, this quick formation cannot be explained by accretion alone, since stellar-mass black holes cannot accrete enough matter in such a short time, even at the maximum allowed accretion rate, the Eddington rate. Although super-Eddington accretion might take place via different mechanisms (e.g., Alexander & Natarajan 2014), the favored scenario for SMBH formation is instead through the merger of seed intermediate-mass black holes (IMBHs), which themselves may form through runaway mergers of stars.

For this reason, much effort has been devoted in recent years to searching for evidence of the existence of IMBHs, focusing on environments where they might have formed, such as in globular clusters. Besides having high enough stellar densities to form IMBHs, globular clusters have velocity dispersions consistent with a low-mass extrapolation of the M – σ relation (e.g., Ferrarese & Merritt 2000), making them good host candidates for IMBHs. In addition to this, they could also have delivered seed IMBHs to the center of galaxies to form SMBHs, since globular clusters are usually about the same age as their host galaxies.

Kains et al. (2016) proposed using gravitational microlensing to achieve an unambiguous IMBH detection, motivated by hitherto-published detections being subject to strong caveats and possible alternative explanations. Indeed, microlensing by an IMBH in the cluster would produce an astrometric deflection to the position of background stars, which, if detected, would then allow us to derive a mass for the IMBH, without relying on any assumption on the nature of the system. This is an

advantage over other techniques; for instance, observations aiming to detect X-ray emission caused by accretion onto an IMBH are reliant on assumed accretion models (Grindlay et al. 2001; Maccarone et al. 2005; Haggard et al. 2013; Mezcua et al. 2015), and cusps in both photometric and kinematic profiles are not unique signatures of the presence of an IMBH in the cluster center (Illingworth & King 1977; Baumgardt et al. 2003; Lanzoni et al. 2007; Ibata et al. 2009; Trenti et al. 2010; Vesperini & Trenti 2010).

In this paper, we report attempts to detect the astrometric deflection that might be caused by an IMBH in the globular cluster M22 on background stars, due to gravitational microlensing. M22 (NGC 6656) was identified by Kains et al. (2016) as the most promising candidate for such a detection, thanks to the combination of a high density of background Galactic bulge stars, a large cluster-bulge relative motion, and, at 3.2 kpc, being one of the closest globular clusters in the Milky Way. This makes the detection of an astrometric lensing event more likely to be achievable over reasonable timescales, given their long typical timescales (~ 3000 days for a $10^4 M_\odot$ IMBH).

In Section 2, we review the basics of astrometric microlensing and how a detection of this effect can lead to a direct mass estimate; in Section 3, we describe the *HST* archival data used for this study and the reduction process. We outline our procedure to model astrometric time series for each star in our sample in Section 4, and we discuss our results in Section 5.

2. Astrometric Microlensing

For a full discussion of astrometric microlensing, we refer the reader to Hog et al. (1995) and Dominik & Sahu (2000). Here, we recall the key equations that are relevant to the work presented in this paper.

Gravitational microlensing occurs when a background source, located at a distance D_S from the observer, becomes sufficiently aligned with a foreground *lens* object at distance D_L . Given a lens of mass M , the Einstein ring radius θ_E gives a typical angular scale for the alignment necessary for microlensing to occur, and is given as

$$\theta_E = \sqrt{\frac{4GM}{c^2}(D_L^{-1} - D_S^{-1})}. \quad (1)$$

Because multiple, nonidentical, images of the source are produced during an microlensing event, but these usually cannot be resolved, we can, instead of the motion of individual images, observe the motion of the source’s centroid as the event unfolds. With the source-lens angular separation u expressed in units of θ_E , one can derive an expression for the astrometric shift $\delta(u)$ that occurs during an microlensing event (Hog et al. 1995) as

$$\delta(u) = \frac{u}{u^2 + 2}\theta_E. \quad (2)$$

Note that this expression assumes a dark lens, i.e., no or negligible blended light from the lens. This gives the total deflection caused by microlensing, which points away from the lens, as seen by the observer, i.e., along a line joining the lens and undeflected source positions.

The components parallel and perpendicular to the source-lens relative motion can be expressed (e.g., Dominik & Sahu 2000) as

$$\begin{aligned} \delta_{\parallel} &= \frac{p}{u_0^2 + p^2 + 2}\theta_E \\ \delta_{\perp} &= \frac{u_0}{u_0^2 + p^2 + 2}\theta_E, \end{aligned} \quad (3)$$

where u_0 is the impact parameter, or minimum source-lens angular separation, in units of θ_E , and $p \equiv p(t)$ is expressed as

$$p = \frac{t - t_0}{t_E}, \quad (4)$$

where t_0 is the time at which $u = u_0$ and t_E is the Einstein timescale, defined as the time taken by the source to cross θ_E . In two dimensions, a source affected by microlensing traces an elliptical motion, in the source’s rest frame, and is relative to its undeflected position, with eccentricity $\epsilon = [2/(u_0^2 + 2)]^{1/2}$ (Dominik & Sahu 2000).

From Equation (1), we see that the mass of the lens, M , can be measured directly if three quantities are determined: the distances to the source and lens, D_S and D_L , and θ_E . Although the lens distance is usually unknown in microlensing events, and can only be constrained when second-order effects can be measured from photometric light curves, such as the parallax effect caused by the Earth’s orbit around the Sun (e.g., Dominik 1998; An et al. 2002; Gould 2004), in the case of an IMBH in the center of a globular cluster, D_L is known, to the extent that the distance to the cluster is known. For Galactic globular clusters, this is usually the case to a precision of a few hundred parsecs (e.g., Harris 1996).

The discussion above assumes that the images are unresolved. However, when considering IMBH lenses, with possible values of θ_E of several hundreds of milliarcseconds for the top end of the IMBH mass range ($>10^5 M_{\odot}$), it is possible that some events may fall in the “partially resolved” regime. In this case, the separation between the source images is large

enough to be resolved with instruments on *HST*, and Equation (2) becomes instead

$$\delta(u)_{\text{pr}} = \frac{1}{2}(\sqrt{u^2 + 4} - u)\theta_E. \quad (5)$$

For values of $u \gtrsim 4$, Equations (2) and (5) converge. In the following discussion of our data and modeling procedure, we will show that here we can safely assume that features in the unresolved microlensing regime.

3. Data and Reduction Process

3.1. Archival Data

We searched the Mikulski Archive for Space Telescopes (MAST) for data that would satisfy several criteria. Images must have been observed in medium- or wideband filters, with the Wide Field Planetary Camera 2 (WFPC2), the Advanced Camera for Surveys (ACS), or Wide Field Camera 3 (WFC3); this is because observations taken with narrowband filters do not go deep enough to enable us to derive precise astrometry for bulge stars. Images must also contain the center of M22 at least $10''$ from the edge of the image and have exposure times long enough to probe background bulge stars located behind the cluster. A summary of the final data set satisfying these criteria, spanning 19.33 years, is given in Table 1.

3.2. Reduction

We reduced available images from data sets given in Table 1 using the suite of tools developed by Jay Anderson (e.g., Anderson & King 2003). For ACS and WFC3 images, we used `flc` images, which are available in the archive and have been corrected for charge-transfer efficiency (CTE) losses. The importance of CTE loss correction has been discussed in several papers; for more details, see, e.g., Bellini et al. (2014).

The first detection and measurement of stars in each image were made using the routine `hst1pass`. When available, a standard point-spread function (PSF) array was used for each instrument/filter combination (Anderson & King 2006); when this was not available, we used the available standard PSF that was closest in wavelength (e.g., for the F547M filter, we used the F467M standard PSF). This is satisfactory because the PSF that is used for the measurement of each star is actually an interpolation of the nearest four PSFs on the image. Furthermore, the time dependence is also accounted for by calculating perturbations to the PSF for each observation. Finally, we also applied the geometric distortion corrections of Anderson & King (2006) to position measurements.

Using an image from the ACS Survey of Galactic Globular Clusters (*HST* Treasury Program; Sarajedini et al. 2007) as a reference, we used `xym2mat` to derive positions in a common coordinate system of all stars in each image. This is done by deriving a six-parameter transformation between an image and the reference, allowing us to measure the position of stars on each transformed image. Applying this transformation to the entire set of available images then yields astrometric time series for each star.

Although transformations were derived for WFPC2/WFC images, these were found to be imprecise, with scatter as large as 1 pixel in most measurements. There are several reasons for this: WFPC2’s larger pixels, its smaller dynamic range, and the lack of dithering typical of early *HST* observations. Due to this, we did not include WFPC2/WFC images in the rest of the

Table 1
HST Archival Data of M22 that Satisfied Our Observing Criteria

Proposal ID	PI	Instrument/Camera	Dates	Filters	Exposure Times
5344	Bailyn (1)	WFPC2/PC	1995 Mar	F439W F675W	40–400 s 10–100 s
*7615	Sahu (2)	WFPC2/WFC	1999 Mar–Jun 1999 Mar–2000 Feb	F606W F814W	260 s 260 s
*8174	Van Altena	WFPC2/WFC	2000 Jun	F555W	26 s
10524	Ferraro	WFPC2/PC	2006 Apr	F555W	30 s
10775	Sarajedini (3)	ACS/WFC	2006 Apr	F606W F814W	55 s 65 s
*11233	Piotto (4)	WFPC2/WFC	2008 Apr	F450W F814W	350 s 100 s
11975	Ferraro	WFPC2/PC	2009 Apr	F555W	10 s
12193	Lee	WFC3/UVIS	2011 May	F467M F547M	361–367 s 75 s
12311	Piotto (5)	WFC3/UVIS	2010 Sep–2011 Mar	F275W F814W	812 s 50 s
13297	Piotto (5)	WFC3/UVIS	2014 Jul	F336W F438W	475 s 141 s

Note. An asterisk in front of the program number denotes WFPC2 data sets that we subsequently excluded (see the text). Reference papers describing the observing programs in detail, when available, are (1) Bailyn et al. (1996), (2) Sahu et al. (2001), (3) Sarajedini et al. (2007), (4) Piotto et al. (2012), (5) Piotto et al. (2015).

analysis. This issue did not affect the planetary camera on WFPC2, and we retain these data for further analysis in addition to ACS and WFC3 data. The excluded data sets were those of proposal IDs 7615 (PI: Sahu), 8174 (PI: Van Altena), and 11233 (PI: Piotto).

3.3. Proper-motion (PM) Corrections

Cluster stars are extremely unlikely to be lensed by another object in the cluster, since for such a case, $D_s/D_L \sim 1$, resulting in a very small Einstein ring radius (Equation (1)). We can therefore assume that cluster stars move in a straight line, i.e., without any microlensing deflections, and use this to correct for systematics that may result in nonrectilinear time series for those stars.

To do this, we fitted straight-line proper motions to the time series of all cluster stars and looked at the distribution of residuals from those fits. For each filter/epoch/instrument, we then computed the median residual from the straight-line fit. In case systematics offsets are present, these median residuals would be nonzero, whereas for random scatter, the distribution of residuals would be centered on zero. For each filter/epoch/instrument, we then subtracted this median offset value from the time series of all stars. We binned data taken with the same instrument in 10 day bins; given the very slow-evolving signals we are looking for in this work, any variation that may happen on 10 day timescales can be ignored without losing significant information on the long-timescale events. Finally, position measurements for different filters were combined at each epoch, producing a single position at each epoch/instrument combination.

3.4. Stars near the Center

We used the center coordinates for the cluster center from Goldsbury et al. (2010), $\alpha = 18.36.23.94$, $\delta = -23:54:17.10$; associated uncertainties are $\pm 0''.8$. Although any IMBH present in the cluster is expected to be located at the center, N -body simulations suggest that it might also be slightly off-center due to interactions between the IMBH and stars in the cluster (de Vita et al. 2018). We therefore selected stars within a radius of

$6''$ of the center for further analysis in order to be conservative in accounting both for uncertainties in the precise location of the center itself and for the amount by which an IMBH might be off-center (de Vita et al. 2018).

The large M22–bulge relative motion of $\sim 12.2 \text{ mas yr}^{-1}$ (Bellini et al. 2014; Kains et al. 2016) makes cluster members easily distinguishable from background bulge stars using their proper motion, derived from initial linear fits to their astrometric time series, as shown in Figure 1. Using this, we identified 8 bulge stars from 199 stars detected on the reference image within $6''$ of the center. Coordinates and PMs for these eight stars are given in Table 2

4. Modeling Procedure

For each star in our sample, we fitted two models:

1. A PM-only model, with parameters μ_x , μ_y , x_0 , and y_0 , respectively the PMs along the x and y directions on the image and arbitrary reference x and y positions
2. An astrometric microlensing model, described by the standard microlensing parameters t_0 , t_E , u_0 , described in Section 2, as well as α , the relative angle of the lens-source trajectories, the Einstein ring radius θ_E , and the PM parameters μ_x , μ_y , x_0 , and y_0 .

Note that the closest star to the cluster center is $\sim 1''.6$ away from the center coordinates of Goldsbury et al. (2010), which means that any microlensing event would either occur in the unresolved regime or be very well approximated by unresolved microlensing models, as long as the Einstein ring radius is less than $\sim 400 \text{ mas}$, which, for a lens in M22 and a Bulge source, corresponds to a $\sim 10^5 M_\odot$ IMBH. We also note here that in the following discussion, we use the term “shift” when referring to microlensing fits and “residuals” when referring to residual positions after subtraction of a PM model.

After fitting both the PM and microlensing models, we compared them using the Bayesian information criterion (BIC; Schwarz 1978), defined as

$$\text{BIC} = -2 \ln(\mathcal{L}) + N_p \ln(N_D) - N_p \ln(2\pi), \quad (6)$$

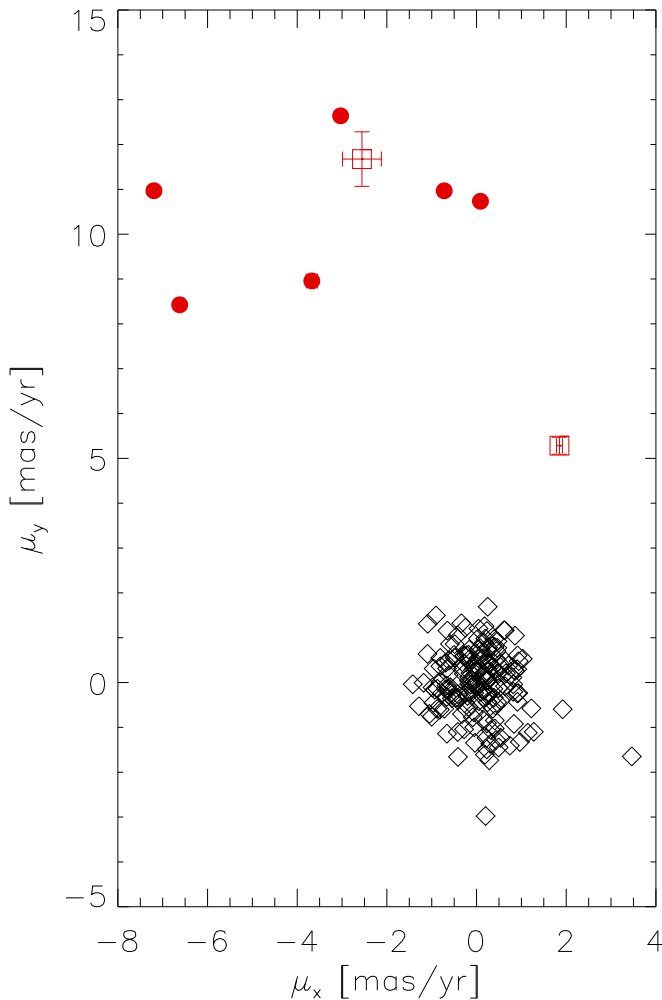


Figure 1. Proper motions derived from initial straight-line fits to astrometric time series. Cluster stars are shown as open diamonds, while bulge stars, clearly separated in the proper-motion diagram, are plotted as filled red circles and open squares (for the two stars with <4 epochs with astrometric measurements), with 1σ error bars (too small to see for most stars).

where \mathcal{L} is the likelihood, N_D is the number of data points (twice the number of epochs, with astrometric measurements, since the position is measured in two directions), and N_P is the number of model parameters (nine for microlensing models, four for PM models). Here, we have assumed constant priors on most parameters, as no information is available from a photometric microlensing light curve fit, for instance (e.g., Kains et al. 2017). However, we do impose a Gaussian prior on the relative source-lens motion, using the cluster-Bulge relative motion $12.2 \pm 3.9 \text{ mas yr}^{-1}$ measured by Kains et al. (2016) from the proper-motion catalog of Bellini et al. (2014). This is particularly important in cases where data are limited, in which case model fits may converge to parameters that are not consistent with the observed relative motion. Using the BIC for the best-fit MCMC models, we then compute their relative probability:

$$\frac{P(\text{PM})}{P(\text{microlensing})} = \exp(0.5(\Delta_{\text{BIC}})), \quad (7)$$

where $\Delta_{\text{BIC}} = \text{BIC}_{\text{microlensing}} - \text{BIC}_{\text{pm}}$. In addition, we impose an additional requirement that an astrometric lensing be at least

1000 times more probable to be favored, which corresponds to a threshold $\Delta_{\text{BIC}} = 13.82$. The BIC is usually most appropriate when $N_D \gg N_P$, but the high additional penalty we impose on the microlensing models means that even with a relatively small number of data points, the BIC is sufficient for the purposes of selecting a model in this work. To test this, we generated PM-only astrometric time series, with scatter corresponding to our real data, and fitted both PM and microlensing models to these simulated data sets. We generated and fitted 1000 such data sets and found that with such a strict penalty on the microlensing models, the “false alarm” rate, i.e., the fraction of these events where the microlensing model is favored over the correct PM model, is negligible ($<0.1\%$).

Since good astrometry could not be extracted from WFPC2/WFC data, this left us with significant gaps in the time series and only eight distinct epochs. To assess whether such coverage would be sufficient to recover lensing parameters, we generated synthetic astrometric time series from a set of input parameters (IMBH mass, source-lens relative motion, microlensing impact parameter). We assumed Gaussian errors on astrometric measurements and scatter consistent with our real data. We then analyzed these synthetic data sets with our modeling codes and found that synthetic astrometric curves allowed us to recover input parameters for a wide range of masses, although with large associated uncertainties, as expected with this few epochs. Figure 2 shows an illustration of one such a fit, for a $10^3 M_\odot$ IMBH, with $t_E = 1900$ days. However, we do find that this time coverage would miss many events caused by having a low mass ($\lesssim 5 \times 10^2 M_\odot$) or a very high mass ($\gtrsim 10^3 M_\odot$), due to their short timescales (most of the event happening in coverage gaps) or inability to distinguish the total motion from the PM-only motion, respectively.

5. Results and Discussion

As expected, all cluster stars are found to be consistent with rectilinear, constant PM-only models. Given the cluster distance of 3.2 kpc, parallax shifts of ~ 0.3 mas are present in the astrometry, corresponding to variations of $\sim 0.6\%$ of a pixel. This is smaller than the astrometric precision we achieve in this study, and we can therefore safely conclude that parallax does not have a significant effect on our results.

Out of eight bulge stars, two had insufficient (<4) epochs with astrometric measurements, due to their close proximity to saturated stars in most images. This leaves six bulge stars with enough data (5–8 epochs) to detect an astrometric microlensing signal. The lensing model is not favored over the PM-only model for any of these six bulge stars.

In Figure 3, we show plots of the time series for the closest star to the center position of Goldsbury et al. (2010), in two dimensions with the PM subtracted, and of the motion in each of the x and y directions, along with the best-fit PM and lensing models.

From Figures 3–4, it is clear that the data are consistent with no microlensing deflection taking place. The PM-only model is strongly favored, and the microlensing fits converge toward very slow-evolving models, which are essentially indistinguishable from PM-only models. These plots are representative of all six bulge stars in our sample.

Although the 10 year gap in our data coverage does not allow us to place strong limits, can we exclude part of the IMBH mass range, based on the lack of detection of an astrometric lensing

Table 2

Coordinates, Proper Motions (along the x and y Image Directions), and Number of Epochs with Astrometric Measurements for the Eight Bulge Stars in Our Sample within $6''$ of the Cluster Center

Star	R.A. (J2000.0)	Decl. (J2000.0)	μ_x (mas yr $^{-1}$)	μ_y (mas yr $^{-1}$)	N_e
1	18:36:24.19	-23:54:18.19	-0.72 ± 0.02	10.97 ± 0.03	8
2	18:36:24.43	-23:54:20.52	-3.67 ± 0.12	8.96 ± 0.02	5
3	18:36:24.35	-23:54:14.04	-7.19 ± 0.02	10.97 ± 0.08	6
4	18:36:24.24	-23:54:12.60	-2.56 ± 0.43	11.68 ± 0.61	3
5	18:36:24.22	-23:54:18.30	-6.62 ± 0.04	8.42 ± 0.02	6
6	18:36:24.13	-23:54:15.00	1.85 ± 0.07	5.28 ± 0.19	4
7	18:36:23.88	-23:54:18.27	-3.03 ± 0.03	12.64 ± 0.05	7
8	18:36:23.87	-23:54:19.19	0.09 ± 0.05	10.73 ± 0.04	8

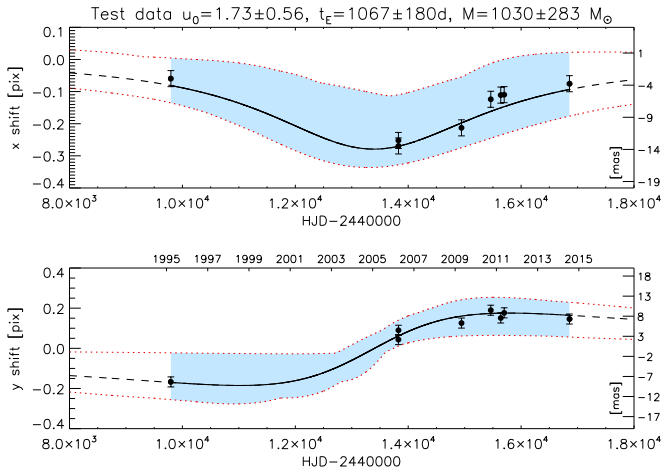


Figure 2. Best-fit model to test data for a $10^3 M_\odot$ IMBH in M22, with $t_E = 1900$ days, $u_0 = 1.5$. The source-lens relative motion is ~ 14 mas yr $^{-1}$. Recovered parameters are in agreement with input parameters, but with large error bars. Blue shaded areas and red dotted lines show the limits of the 99.7% confidence interval. The top axis in the bottom panel gives the time in calendar years.

signal in those six stars? From McLaughlin & van der Marel (2005), the larger estimate for the total mass of M22 is $\log_{10}(M_{\text{tot}}/M_\odot) \approx 5.64 \pm 0.05$. Therefore, an extreme scenario in which an IMBH makes up $\sim 10\%$ of the total cluster mass would mean an IMBH with $\log(M_{\text{tot}}/M_\odot) \approx 4.64$. How far down the IMBH mass range would a black hole (BH) have caused a detectable event, given our data?

To estimate this, we carried out Monte Carlo simulations, first placing a BH at a location near the center, with variation in the BH location given due to the uncertainty in the precise location of the center (Goldsbury et al. 2010), as well as potential IMBH “wander,” the size of which is $M_{\text{BH}}^{-0.44}$ (de Vita et al. 2018). Given a BH position, the actual location of a bulge star at observed times, as well as the star’s observed motion relative to the cluster (and thus BH), we then derived lensing parameters. Using these, we calculated the expected astrometric deflection at each observed epoch and determined whether such a deflection would have been detected, given our astrometric measurements.

If so, our data allow us to exclude the presence of such a BH at the center of M22. This was repeated for 10^5 random BH locations and masses, after which we calculated the detection

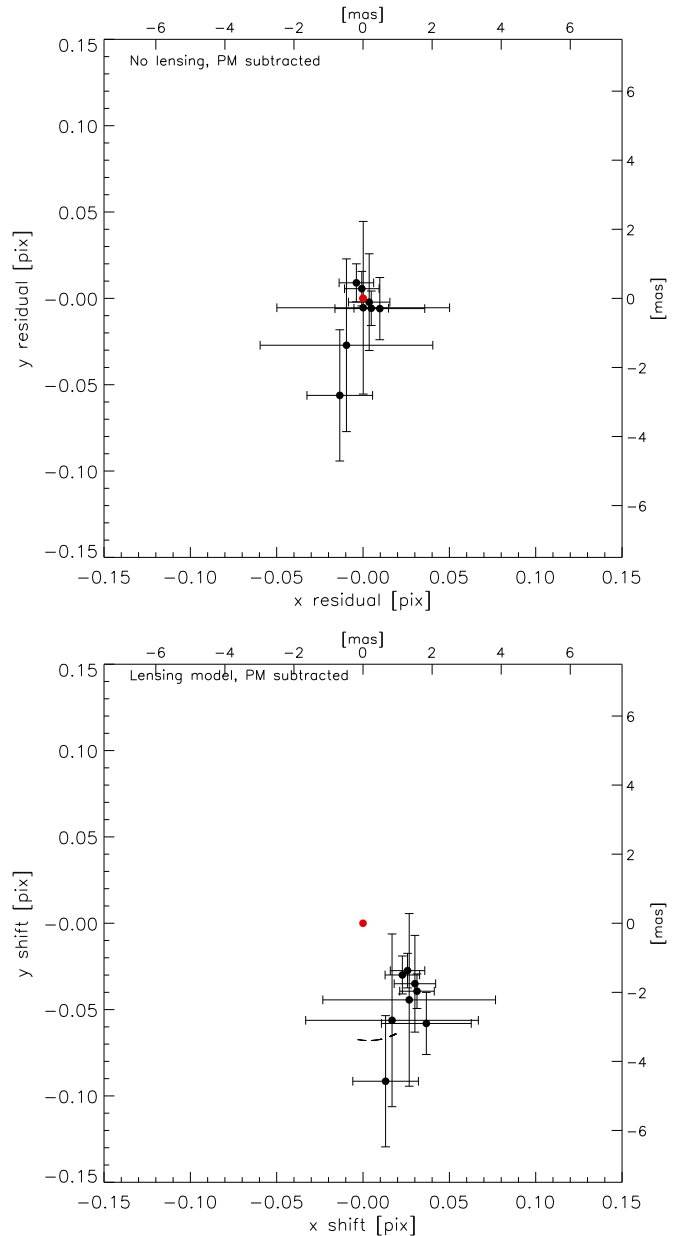


Figure 3. Two-dimensional residual positions after proper-motion subtraction, for the PM-only model (top) and astrometric microlensing model (bottom), for the closest star to the center of M22.

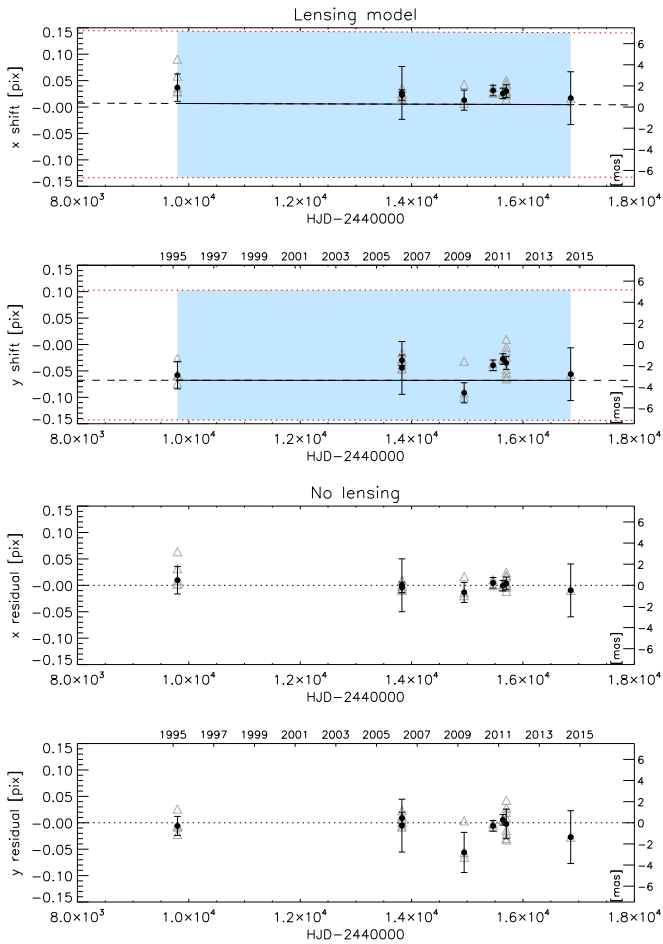


Figure 4. Residual positions after proper-motion subtraction, for each of the x and y pixel positions, for the PM-only model (top) and astrometric microlensing model (bottom), for the closest star to the center of M22. For the microlensing model, the best-fit model to the microlensing shift over the 19.33 year baseline is also plotted as a solid line, and the blue shaded areas and red dotted lines show the limits of the 99.7% confidence interval. For each model, a time axis in calendar years is shown between the two panels. Individual-image measurements are shown as gray open triangles, while combined measurements are plotted as filled circles with error bars.

rate as a function of BH mass, giving us an estimate of the maximum BH mass that would have produced a given detection rate. This is plotted in Figure 5 for the closest star to the cluster center. For that star, the detection rate rises steadily as a function of mass, due to the small impact parameter, meaning that high-mass BH events would have been detected despite unfolding slowly. A 50% detection rate corresponds to a BH mass of $\sim 22\%$ of the total cluster mass, while for a BH mass of 10% and 1% of the cluster mass, the detection rates would be $\sim 16\%$ and 2% , respectively. Finally, we also estimated the detection rates, adding a data point every two years over our coverage gap (1996–2005), with an error bar corresponding to the median error in our data set, and Gaussian scatter around a straight-line source trajectory, to assess the improvement from having better time coverage. For the simulated data sets, we find a 50% detection rate at $M \sim 0.12M_{\text{cluster}}$, as well as 42% and 2% for BH masses of 10% and 1% of the total cluster mass, respectively. As expected, more regular time coverage improves detection rates significantly for higher masses

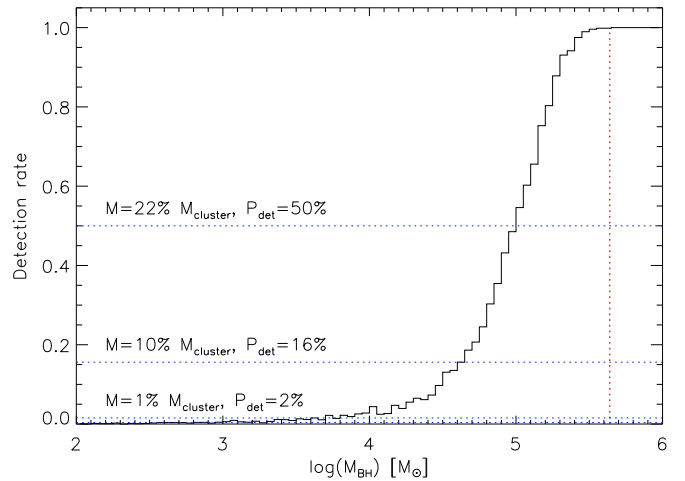


Figure 5. Detection rates as a function of BH mass, given the actual astrometric time-series data, for the star closest to the center of M22. The vertical dotted red line shows the total cluster mass from McLaughlin & van der Marel (2005), while horizontal lines show detection rates of 50%, as well as for masses corresponding to 10% and 1% of the total cluster mass. Note that an event being detected does not mean that the lens mass can be recovered; see Figure 6 for an estimate of the probability of events being detected *and* that have the BH mass recovered.

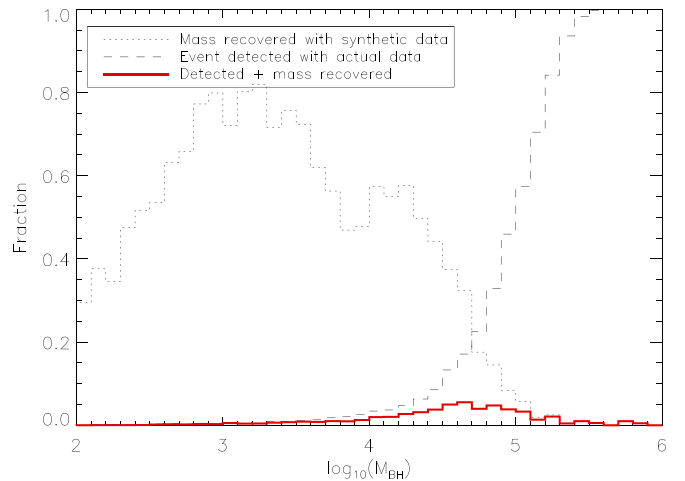


Figure 6. Mass recovery rate (dotted line), detection rate (dashed line), and the product of these two, giving the rate of events that are detected and have their BH mass recovered, as a function of BH mass.

($\gtrsim 10^4 M_{\odot}$), whereas more frequent observations are needed to improve detection rates at lower masses ($\lesssim 10^4 M_{\odot}$).

In addition to detecting an event caused by the presence of the BH in the cluster, how often can we also recover the mass of the BH, given our time sampling? We can use simulated data (e.g., Figure 2) to estimate how the mass recovery rate changes with BH mass, assuming the time coverage of our data set. We did this by generating synthetic data sets, fitting these with our astrometric modeling code and comparing the fitted parameters to the input parameters. In this case, we considered the mass recovered when the fitted mass was within 0.5 dex of the input mass. In Figure 6, we plot the mass recovery rate, detection rate, and the multiplication of these two, giving the rate of events that are detected *and* for which the mass is recovered. We find that given our data, only BH with masses between 10^4 and $10^5 M_{\odot}$ have a significant chance of both being detected and having their mass recovered, between $\sim 3\%$ and 6% . This

is because higher-mass events, while they can be detected because of the large signal they produce, are slow-evolving, leading to mostly rectilinear deflections on timescales of approximately years; these do not provide good constraints on the lens masses. On the other hand, lower-mass events can be better modeled thanks to less rectilinear deflection signals, but are less easily detected because of the smaller signals they produce.

Finally, we checked the catalog from the *Gaia* (Gaia Collaboration et al. 2016) data release 2 (DR2; Gaia Collaboration et al. 2018) for matches to the bulge stars in our sample to compare our derived PMs with DR2 values. Indeed, in the most extreme cases involving a background star being deflected by a very massive BH, with a low impact parameter, a trajectory might appear rectilinear over even a 20 year baseline, but could actually be a small fraction of a lensing event. In such a case, the true direction of the star's PM would be different from that derived from the observations, and a second set of later observations might reveal a change in direction, hinting at a possible microlensing taking place. Although this would be unlikely to be seen from *Gaia* data, since they only span 22 months of data from 2014 July to 2016 May, whereas our archival data set ends in 2014, we considered this possibility for thoroughness. Unfortunately, only three of our bulge sources had *Gaia* matches at a distance $<1''$, and none of these three had PM values in DR2. However, this is a check worth making when considering the possibility of astrometric microlensing by very massive BHs.

6. Conclusions





Using *HST* archival data spanning nearly 20 years of baseline, we derived astrometric time series for 199 stars within $6''$ of the center of M22, but with a large 10 year gap, due to being unable to extract high-precision astrometry from the WFC chips of the WFPC2 instrument. This includes six bulge stars with sufficient time coverage to detect microlensing signals, if present, and constrain the lens properties. These six stars do not show any signatures of microlensing deflections and are consistent with PM-only models. Although in theory it is possible to use these nondetections to place limits on the mass of any IMBH present at the cluster center, the insufficient precision of WFPC2/WFC astrometry led to a large gap in time coverage that meant we were unable to derive any useful limits for realistic BH masses.

We conclude that it is worth extending this work to other clusters, particularly those with rich *HST* archival data sets, such as M 4 or 47 Tuc. The tools developed in this study will make future analyses of other clusters much faster. In addition, the astrometric microlensing analysis tools we wrote as part of this project would also be useful in preparation for the *Wide Field Infrared Survey Telescope's* (WFIRST) microlensing Survey, for which astrometry has the potential to significantly improve the constraints yielded by the survey on lens masses (Gould & Yee 2014), including on the mass function of stellar-mass BHs and extrasolar planets. In addition, it will be worth revisiting models in the future, for instance after observations of the centers of these clusters have been taken by the *James*

Webb Space Telescope (JWST), which will afford even better astrometric precision than what is currently achievable with *HST*.

Support for this work was provided by NASA through grant number AR-14571 (PI: Kains) from the Space Telescope Science Institute, which is operated by AURA, Inc., under NASA contract NAS 5-26555. Based on observations made with the NASA/ESA *Hubble Space Telescope*, obtained by the Space Telescope Science Institute. All of the data presented in this paper were obtained from the Mikulski Archive for Space Telescopes (MAST).

ORCID iDs

N. Kains  <https://orcid.org/0000-0001-8803-6769>
 A. Calamida  <https://orcid.org/0000-0002-0882-7702>
 K. C. Sahu  <https://orcid.org/0000-0001-6008-1955>
 J. Anderson  <https://orcid.org/0000-0003-2861-3995>

References

- Alexander, T., & Natarajan, P. 2014, *Sci*, 345, 1330
 An, J. H., Albrow, M. D., Beaulieu, J.-P., et al. 2002, *ApJ*, 572, 521
 Anderson, J., & King, I. R. 2003, *AJ*, 126, 772
 Anderson, J., & King, I. R. 2006, ACS/ISR 2006-01 (Baltimore, MD: STScI) <http://www.stsci.edu/hst/acs/documents/isrs>
 Bailyn, C. D., Rubenstein, E. P., Slavin, S. D., et al. 1996, *ApJL*, 473, L31
 Baumgardt, H., Hut, P., Makino, J., McMillan, S., & Portegies Zwart, S. 2003, *ApJL*, 582, L21
 Bellini, A., Anderson, J., van der Marel, R. P., et al. 2014, *ApJ*, 797, 115
 de Vita, R., Trenti, M., & MacLeod, M. 2018, *MNRAS*, 475, 1574
 Dominik, M. 1998, *A&A*, 330, 963
 Dominik, M., & Sahu, K. C. 2000, *ApJ*, 534, 213
 Fan, X. 2006, *NewAR*, 50, 665
 Ferrarese, L., & Merritt, D. 2000, *ApJL*, 539, L9
 Gaia Collaboration, Prusti, T., de Bruijne, J. H. J., et al. 2016, *A&A*, 595, A1
 Gaia Collaboration, Brown, A. G. A., Vallenari, A., et al. 2018, arXiv:1804.09365
 Goldsbury, R., Richer, H. B., Anderson, J., et al. 2010, *AJ*, 140, 1830
 Gould, A. 2004, *ApJ*, 606, 319
 Gould, A., & Yee, J. C. 2014, *ApJ*, 784, 64
 Grindlay, J. E., Heinke, C., Edmonds, P. D., & Murray, S. S. 2001, *Sci*, 292, 2290
 Haggard, D., Cool, A. M., Heinke, C. O., et al. 2013, *ApJL*, 773, L31
 Harris, W. E. 1996, *AJ*, 112, 1487
 Hog, E., Novikov, I. D., & Polnarev, A. G. 1995, *A&A*, 294, 287
 Ibatova, R., Bellazzini, M., Chapman, S. C., et al. 2009, *ApJL*, 699, L169
 Illingworth, G., & King, I. R. 1977, *ApJL*, 218, L109
 Kains, N., Bramich, D. M., Sahu, K. C., & Calamida, A. 2016, *MNRAS*, 460, 2025
 Kains, N., Calamida, A., Sahu, K. C., et al. 2017, *ApJ*, 843, 145
 Lanzoni, B., Sanna, N., Ferraro, F. R., et al. 2007, *ApJ*, 663, 1040
 Maccarone, T. J., Fender, R. P., & Tzioumis, A. K. 2005, *MNRAS*, 356, L17
 McLaughlin, D. E., & van der Marel, R. P. 2005, *ApJS*, 161, 304
 Mezcuca, M., Roberts, T. P., Lobanov, A. P., & Sutton, A. D. 2015, *MNRAS*, 448, 1893
 Piotto, G., Milone, A. P., Anderson, J., et al. 2012, *ApJ*, 760, 39
 Piotto, G., Milone, A. P., Bedin, L. R., et al. 2015, *AJ*, 149, 91
 Sahu, K. C., Casertano, S., Livio, M., et al. 2001, *Natur*, 411, 1022
 Sarajedini, A., Bedin, L. R., Chaboyer, B., et al. 2007, *AJ*, 133, 1658
 Schwarz, G. 1978, *AnSta*, 21, 461
 Trenti, M., Vesperini, E., & Pasquato, M. 2010, *ApJ*, 708, 1598
 Vesperini, E., & Trenti, M. 2010, *ApJL*, 720, L179